Journal of Alloys and Compounds 927 (2022) 166908

Contents lists available at ScienceDirect

Journal of Alloys and Compounds

journal homepage: www.elsevier.com/locate/jalcom

Highly stable honeycomb structured 2D/2D vanadium aluminum carbide MAX coupled g-C_3N_4 composite for stimulating photocatalytic CO_2 reduction to CO and CH_4 in a monolith photoreactor

Beenish Tahir[b,c], Muhammad Tahir[a,*], Mohd Ghazali Mohd Nawawi[c]

[a] Chemical and Petroleum Engineering Department, UAE University, P.O. Box 15551, Al Ain, United Arab Emirates
[b] Civil and Environmental Engineering Department, UAE University, P.O. Box 15551, Al Ain, United Arab Emirates
[c] School of Chemical and Energy Engineering, Universiti Teknologi Malaysia, 81310, UTM, Johor Bahru, Johor, Malaysia

ARTICLE INFO

Article history:
Received 26 April 2022
Received in revised form 20 August 2022
Accepted 23 August 2022
Available online 27 August 2022

Keywords:
Photocatalytic CO_2 reduction
Vanadium aluminum carbide (V_2AlC)
G-C_3N_4
Monolith photoreactor
2D/2D Nanocomposite

ABSTRACT

Developing efficient materials for photocatalytic conversion of CO_2 to value added chemicals and fuels has gained significant attractions in the recent years. However, this is still a difficult task. In this work, a well-designed vanadium aluminum carbide (V_2AlC) MAX coupled with porous graphitic carbon nitride (g-CN) to construct a nanocomposite for photocatalytic CO_2 reduction has been investigated. 2D/2D V_2AlC/g-CN performance was conducted in a fixed-bed and monolith photoreactor under UV and visible light. The V_2AlC/g-CN exhibited photoactivity of 1747 and 67 μmol g^{-1} h^{-1} for CO and CH_4 evolution, which were 4.13 and 1.94 folds more than their production compared to using pristine g-CN, respectively. More importantly, among the sacrificial reagents such as H_2O, CH_3OH, and H_2, the highest productivity was obtained using CO_2-CH_3OH due to more attachment of methanol over g-C_3N_4 with more proton generation. Similarly, performance of V_2AlC/g-CN under UV-light was promising due to the ability of long pathways to penetrate light inside the fixed bed reactor. In addition to photocatalysts, the performance comparison of reactors confirms that the monolith photoreactor has higher productivity for CO_2 reduction to CO and CH_4. This was evidently due to the large illuminated active surface area, and more light utilization, and proficient mass transfer inside the monolithic microchannels. The stability examination further confirms the unceasing evolution of CO and CH_4 in the consecutive four cycles. Thus, V_2AlC MAX is a promising layered material and can be coupled with semiconductors as a support or cocatalyst to achieve both photoactivity and stability for continuous fuel production.

1. Introduction

The release of carbon dioxide (CO_2) greenhouse gas due to the burning of naturally reserved fuels has caused two major concerns: global warming and the depleting of natural reservoirs [1]. The demand for cleaner fuels with the utilization of atmospheric CO_2 has generated a strong desire for artificial photocatalysis [2]. For this purpose, different photocatalysts including TiO_2, Cu_2O, CdS, ZnO and WO_3 were explored to get various photochemically generated compounds such as CO, CH_4, CH_3OH and HCOOH during the CO_2 photoreduction process [3–7]. All these materials have limitations in terms of lower efficiency or functionality under UV-light irradiation. Thus, the advancement of efficient, stable, and selective materials for CO_2 reduction is highly demanding but has remained a great challenge [8].

Two-dimensional (2D) noble metal free materials such as graphitic carbon nitrides (g-C_3N_4) due to several advantages, such as ease of preparation, active under UV/visible light irradiation, higher reduction potential, and less hazard to the environment, have been investigated by many researchers [9,10]. Among the g-C_3N_4 benefits, it has lower efficiency due to charge recombination in the layered structure, less specific surface area, and poor conductivity [11,12]. To promote photocatalytic activity, several strategies have been investigated over the years including metal loading (Ag, Au, Ni, Cu and Co) [13–15], non-metal loading (S, O, P and B) and constructing heterojunction with other semiconductors [16,17]. For example, C and Ag were loaded with g-C_3N_4 and reported increasing trends in CO_2 photoreduction due to higher light absorption, providing more

Abbreviations: Carbon Dioxide, CO_2; Vanadium Aluminium Carbide, V_2AlC; Titanium Dioxide, TiO_2; Graphitic Carbon Nitride, g-C_3N_4; Powder X-ra y diffraction, XRD; Vanadium Carbide, V_2C

* Corresponding author.
E-mail addresses: muhammad.tahir@uaeu.ac.ae, bttahir@yahoo.com (M. Tahir).

https://doi.org/10.1016/j.jallcom.2022.166908
0925-8388/

active sites and good charge separation [18]. Similarly, Ni-Ag loaded g-C_3N_4 was explored with an obvious increment in H_2 yield due to faster photogenerated charge separation [19]. In another work, B, O, B and P non-metals were loaded with g-C_3N_4 and reported obvious increment in CH_4 evolution during CO_2 reduction [20]. Similarly, $BiOIO_3$/g-C_3N_4 heterojunction was tested for solar light activated CO_2 conversion with CO and CH_4 as the potential products [21]. In the present advancement, biochar [22] and MAX materials are under examination to replace expensive metals and semiconductors by providing another alternative solution in nanomaterials [23].

The MAX is made up of three elements: M (early transition metals), A (group III or IV A element), and X (either C or N). Thus, MAX belongs to the carbide or nitrides family and has general formula $M_{n+1}AX_n$, where n can be either 1, 2 or 3 [24]. MAX and MXenes are different from other materials because they are thermal and mechanical stability and have good electrical and thermal conductivity. They are widely used in many different ways such as energy storages, batteries, electrical conductors, and as cocatalysts [25]. Different types of 2D MAX materials such as Ti_3AlC_2, Ti_2AlC, V_2AlC, and Nb_2AlC have been tested for different applications [26]. Recently, we tested 2D Ti_3AlC_2 supported g-C_3N_4 heterojunction and observed an enhanced CO_2 methanation process due to preventing chargs recombination [27]. Similarly, Ti_3AlC_2/TiO_2 was explored for photocatalytic bi-reforming of methane with synthesis gas production [28]. However, there is another important MAX V_2AC with good conductivity, higher visible light absorption but there is no significant development for employing in photocatalytic applications [29]. For example, recently, V_2C MXene as a support was tested for oxygen reduction and observed to have significantly enhanced performance in a fuel cell [30]. Thus, constructing V_2AlC and g-C_3N_4 2D/2D heterojunction would be promising to promote light-absorption with higher separation of charges to maximize CO_2 reduction efficiency.

In addition to efficient photocatalysts, photocatalytic CO_2 reduction efficiency and selectivity can be significantly altered by using an appropriate design of photoreactor [2]. Among the different designs, monolith photoreactor is highly recommended due to its several benefits. The distinguished features of monolithic-based supports are larger exposed surface area, higher surface to volume ratio, efficient light penetration, lower mass transfer limitations, and faster reaction kinetics [31]. Recently, we investigated the monolith photoreactor for photocatalytic dry reforming of methane over a montmorillonite loaded TiO_2 photocatalyst and found promising photoactivity and product selectivity for CO and H_2 production [32]. In another development, MAX/TiO_2 photocatalysts were tested for converting CO_2 to CO/CH_4 while employing fixed-bed and monolith photoreactors. Similarly, in other developments, the monolith photoreactor was explored with the use of Fe-MMT/TiO_2 [31] and Ni-MMT/TiO_2 [32] nanocomposites with promising results during different CO_2 reduction processes.

Herein, a well-designed vanadium aluminum carbide supported graphitic carbon nitride (V_2AlC/g-CN) nanocomposite was examined for photo-induced CO_2 reduction under UV and visible light irradiations. The composite performance was tested through various parameters such as the effect of light sources, type of sacrificial reagents, and reaction time. It is perceived that hole scavenger has an important effect on encouraging composite photocatalyst photoactivity for selective CO_2 reduction. Similarly, the light source has a significant effect on the photocatalyst performance due to different penetration depth and absorption ability. The composite photocatalyst performance was further explored with fixed-bed and monolith reactors, and their performance was systematically investigated. The stability test in multiple cycles was conducted, which further confirmed higher photoactivity and stability for consecutive four cycles. This work would be fruitful for further investigation in the production of cleaner fuels through the CO_2 reduction process.

2. Experimental

2.1. Materials

The materials and chemicals used in this study are melamine (Merck, 99.99%), methanol (Merck, 99.99%) and vanadium aluminum carbide (V_2AlC, > 98%, 200 mesh, Famouschem China). Similarly, monolith dimensions are 20 mm in diameter and 60 mm in length. The cordierite structure monoliths were purchased from Pingxiang Meitao Company, China.

2.2. Synthesis of mesoporous g-C_3N_4

The bulk graphitic carbon nitride (g-C_3N_4) was synthesized using the thermal decomposition of melamine under air an atmosphere. Specifically, 5 g of melamine placed in a ceramic crucible was covered with a lid and heated at 550 °C for 120 min. The yellow cake obtained was further grinded to fine a powder and stored in an air tight bottle.

2.3. Synthesis of V_2AlC/g-C_3N_4

The vanadium aluminium carbide dispersed graphitic carbon nitride (V_2AlC/g-CN) nanocomposite was synthesized using an ultrasonic assisted physical mixing method. To create a 2D layered structure, 50 mg g-C_3N_4 was displaced into a 20 mL methanol and stirred for 6 h. In parallel, specific amount of V_2AlC exfoliated with 20 mL methanol was transferred to the above suspension under stirring. After stirring for another 6 h, the slurry was oven dried at 100 °C and was given the name V_2AlC dispersed g-CN. The V_2AlC/g-CN samples with different V_2AlC loading amounts, such as 5, 10, and 15 wt%, were prepared using a similar procedure and were named as 5 V_2AlC/g-CN, 10 V_2AlC/g-CN, and 15 V_2AlC/g-CN, respectively. The schematic synthesis illustration for the V_2AlC/g-CN nanocomposite has been shown in Fig. 1.

2.4. Synthesis of monolithic V_2AlC/g-C_3N_4

The monolithic V_2AlC/g-C_3N_4 samples were prepared using the dip-coating method as discussed previously [28]. Initially, monoliths of specific sizes were washed with acetone and methanol to eradicate any impurities. Afterwards, the V_2AlC/g-C_3N_4 suspension was prepared by adding suitable amounts of g-C_3N_4 and V_2AlC as discussed previously. The initial weight of the monolith after drying at 100 °C and cooling to room temperature was measured before starting the coating process. For loading catalysts over the monolith surface and inside the microchannels, the monolith was dipped into the suspension for a few seconds and was gently removed and dried using compressed air. This synthesis procedure was repeated to get a uniform coating of catalyst over the entire surface of monolithic support. After drying at 100 °C, the final weight of the coated monolith was measured and was given the name monolithic V_2AlC/g-CN nanocomposite. The schematic synthesis representation for the monolithic V_2AlC dispersed g-CN composite has been discussed in Fig. 1.

2.5. Characterization

Powder X-ray diffraction (XRD) patterns were recorded with a Rigaku Smart Lab machine, operated at 30 kV, 40 mA, with Cu Kα radiation (λ = 0.154 nm). The morphology and structure of the materials were observed using FESEM with a Hitachi SU8020 instrument. The EDX mapping analysis was conducted to confirm the uniform distribution of elements in the composite. The materials interface interaction was further investigated using high a resolution transmission electron microscope (HRTEM, HITACHI HT7700). The

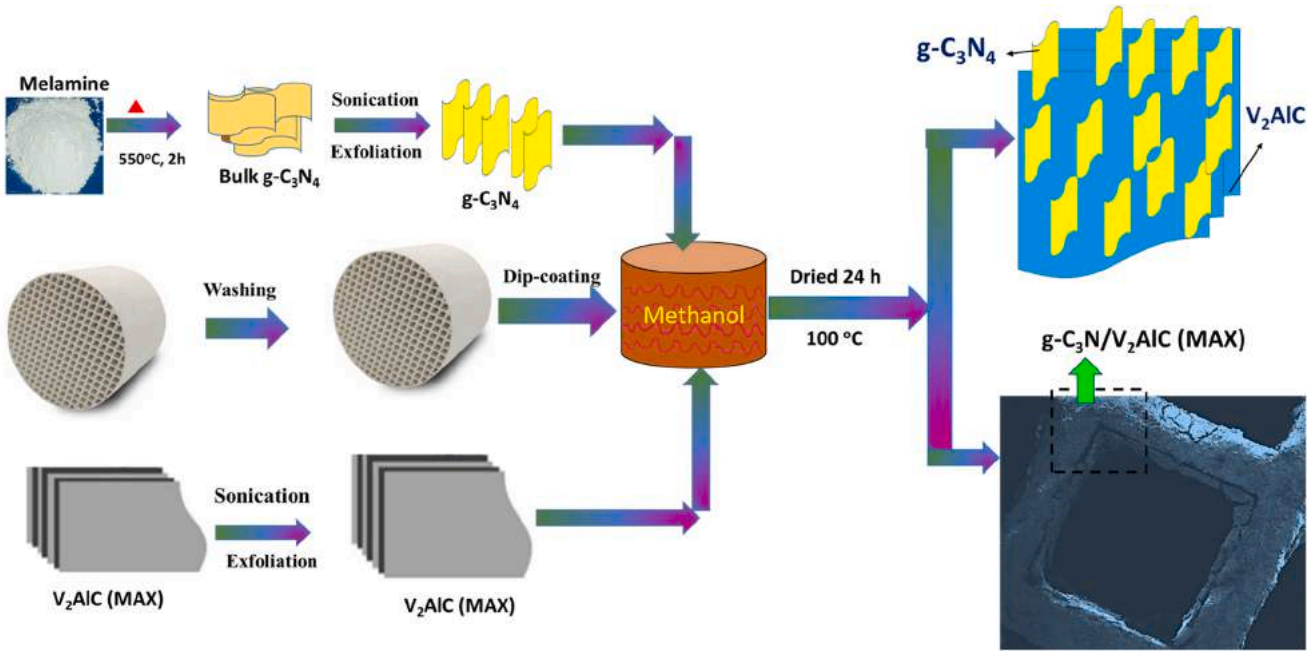

Fig. 1. Schematic synthesis illustration for the V_2AlC loaded g-C_3N_4 and coated over the monolithic support.

elemental composition was measured using X-ray Photoelectron Spectroscopy (XPS) using Axis Ultra DLD Shimadzu electron spectrometer. The RAMAN and PL analyses were conducted using a HORIBA spectrometer with a laser wavelength of 532 and 325 nm, respectively. The UV–visible diffuse reflectance (UV-Vis DR) absorption spectra were obtained using an Agilent Carry 100 spectrophotometer.

2.6. Photocatalytic Activity

The V_2AlC-loaded g-CN nanocomposite performance for photocatalytic CO_2 reduction was conducted in a fixed bed and monolith photoreactor under UV and visible light irradiation [28]. The detailed description of both types of photoreactors is demonstrated in our previous work [32]. The reactor consists of a stainless chamber integrated with mass flow controllers (MFC) and cooling fans to remove lamp heat. A UV-light source was a 200 W Hg lamp having an intensity 100 mW cm^{-2} and wavelength of 254 nm. However, for the visible light source, a 300 W Xenon reflector lamp with intensity 100 mW cm^{-2} and wavelength of 420 nm was employed. Both the lamps were used without employing UV and visible light cut filters. The monoliths used have a size of 2 cm in length and 6 cm in width and channels per square inch (CPSI) of 200. For both the fixed bed and monolith photoreactors, a similar reactor chamber was employed for the best performance companion.

The specific powder photocatalyst amount (0.15 g) was loaded inside the photoreactor system and was cleaned with a constantly flowing helium gas for 30 min. The compressed CO_2 was allowed to flow through the water saturator to carry moisture before entering the reactor. The catalyst bed was saturated with CO_2 and water by continuously flowing the feed mixture for 30 min. For investigating the effect of hole scavenger, 5% methanol and pure hydrogen were employed. Whereas, the methanol solution was replaced with water in a water saturator to investigate the effect of alcohol. Similarly, a CO_2 and H_2 feed mixture was introduced to the reactor chamber with a CO_2/H_2 ratio of 1.0 to investigate the effect of hydrogen. For investigating the CO_2 photoreduction in a monolith reactor, a similar procedure was adopted. However, monolithic supports coated with the catalysts were inserted inside the reactor chamber. The gaseous products were analyzed using gas chromatography (GC), equipped with TCD and FID detectors. The Carboxen-1010 PLOT capillary column was connected to both the detectors for the identification of CO, CH_4, H_2 and CO_2 products.

3. Results and discussion

3.1. Materials Characterization

The XRD analysis was conducted to the confirm phase structure and crystallinity of the pure and the composite samples as presented in Fig. 2(a). The differential peaks for V_2AlC were identified at 2θ of 13.41°, 27.07°, 35.46°, 41.11°, 55.41°, and 63.81°, matching typical (002), (004), (100), (103), (106), and (110) crystal planes of V_2AlC MAX and similar observations were obtained previously [33]. This confirms the high purity of V_2AlC MAX phase with a crystalline structure. The two diffraction peaks at 2θ of 12.91° and 27.41° were identified, fitting to typical crystal planes (100) and (002) of g-C_3N_4. There have been reports of similar results before [34]. When the V_2AlC was coupled with g-CN, all the original peaks were observed, which confirms the effective fabrication of the V_2AlC/g-CN nanocomposite. More importantly, no shifts in peaks were observed in the composite samples, which further confirms original reflections of the phase structure.

The Raman characterization was further performed to confirm the successful fabrication of the V_2AlC dispersed g-CN nanocomposite as presented in Fig. 2(b-c). The V_2AlC reflects obvious peaks at 254 and 352 cm^{-1}, which are the characteristics of pure V_2AlC. Using g-C_3N_4 samples, significant Raman signals were not observed, whereas several characteristic peaks at 475, 703, and 1234 cm^{-1}were detected. Two peaks located at 475 cm^{-1} and 1234 cm^{-1} reflect the vibration modes of CN heterocycles in g-C_3N_4 [35]. Furthermore, the intense peak at 703 cm^{-1} was attributed to the tri-s-triazine ring. Raman spectrum of g-C_3N_4 confirms high purity material with specific graphitic carbon nitride characteristics. There have been similar observations before [36]. When V_2AlC was coupled with g-CN, all the g-CN original peaks exited, but V_2AlC peaks were demised due to lower intensity. More importantly, the one important peak of V_2AlC at 354 cm^{-1}, which confirms the existence of this material in

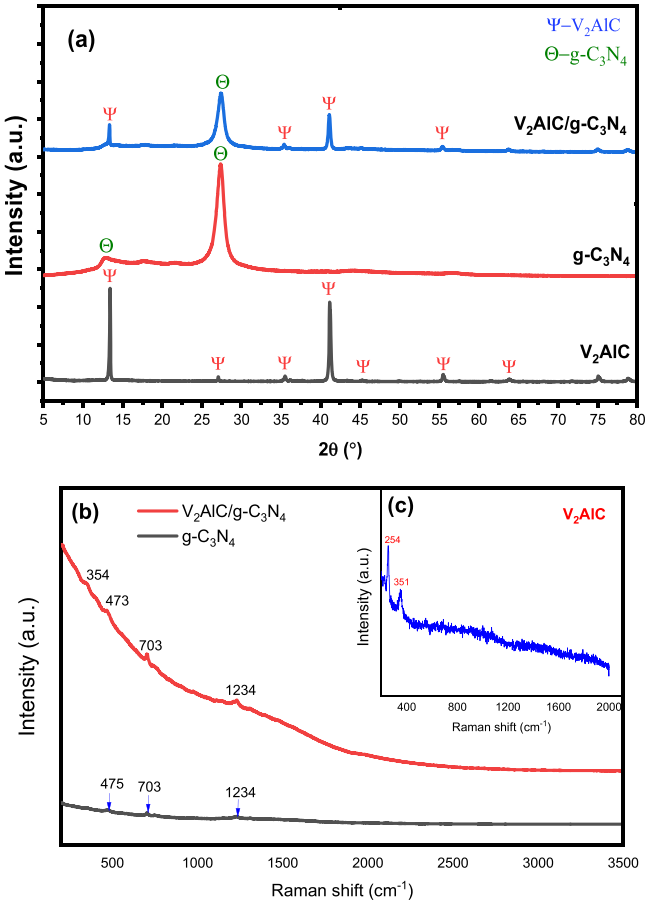

Fig. 2. (a) XRD analysis of pure and V_2AlC loaded g-C_3N_4 samples; (b-c) Raman spectra of V_2AlC, g-C_3N_4 and V_2AlC loaded g-C_3N_4 samples.

the composite. All of these findings support successful fabrication of the V_2AlC dispersed g-CN nanocomposite.

The structure and morphology of g-CN, V_2AlC, and V_2AlC dispersed g-CN were investigated using a Field Emission Scanning Electron Microscope (FESEM) and the images are presented in Fig. 3. Fig. 3(a) shows the layered structure of g-C_3N_4 in which all the sheets have an exfoliated structure. Fig. 3(b) presents a SEM image of V_2AlC, in which compact 2D layers are obvious. However, the exfoliated 2D layered structure of V_2AlC was obtained after exfoliation, as evidenced in Fig. 3(c). When g-C_3N_4 and V_2AlC were coupled together, a good interface interaction was achieved, as demonstrated in Fig. 3(d-e). It is obvious that g-CN sheets are entirely dispersed over the V_2AlC surface, thus, providing good interface interaction. The distribution of elements was further confirmed through EDX mapping, and the results are discussed in Fig. 3(f-j). Fig. 3(f) shows the mapping analysis of V_2AlC/g-CN, in which the distribution of all the materials could be observed. More importantly, the distribution of elements in Fig. 3(g-j) further confirms the uniform distribution of V, Al, C, and N in the V_2AlC/g-CN composite.

The morphology of V_2AlC-loaded g-C_3N_4 was further investigated using TEM and the results are presented in Fig. 4. Pure V_2AlC shows bulk sheets with a 2D structure as shown in Fig. 4(a). The interaction between the V_2AlC and g-CN was further examined and the results are presented in Fig. 4(b-c). It was observed that g-C_3N_4 is successfully dispersed with V_2AlC sheets, giving good interface interaction. The existence of V_2AlC was further confirmed by high resolution TEM analysis and the results are presented in Fig. 4(d). The D-spacing of 0.25 nm was observed by V_2AlC, whereas, D-spacing of g-C_3N_4 was not identified due to its amorphous structure [37]. In general, the V_2AlC/g-CN were coupled together with good interface interaction that would be beneficial to transport charge carriers.

XPS analysis was conducted in order to investigate the elemental composition of the V_2AlC/g-C_3N_4 composite and the results are presented in Fig. 5. Fig. 5(a) shows C1s spectra with four characteristic peaks positioned at 283.2 eV, 284.8 eV, 286.8 eV, and 288.6 eV, ascribed to C-V, C-C, C-O and N-C=N, respectively [38]. The XPS spectrum of Al 2p in Fig. 5(b) shows one broad peak with a binding energy of 74.6 eV, which confirms the presence of Al associated with the MAX phase structure of V_2AlC. Fig. 5(c) shows the V 2p spectrum having a binding energy of 516.9 eV, confirming the existence of V as V^{4+} [37]. The XPS spectrum of N1s in Fig. 5(d) shows three peaks with binding energies of 397.6 eV, 399.1 eV, and 400.1 eV, respectively, ascribed to Sp^2-hybridized nitrogen, N-C_3 and amino functional group (C-NH_2), respectively. All these results confirm the successful fabrication of the V_2AlC/g-C_3N_4 composite without any change in structure or oxidation of the materials.

The color images of the synthesized photocatalysts are depicted in Fig. 6(a-c). The pure V_2AlC reflects a blackish color, g-C_3N_4 has a yellowish color, and V_2AlC loaded g-C_3N_4 shows greyish color due to the presence of V_2AlC. The production and separation of the charges were further investigated using photoluminescence (PL) analysis, and the results are presented in Fig. 6(a). Using pure g-CN, the highest PL peak intensity was observed, which reflects, more charge carrier recombination within the g-C_3N_4 layered structure. More importantly, the PL intensity of pure V_2AlC approaches to straight line due to its conductive characteristics. When V_2AlC was coupled with g-CN, an obvious decline in PL intensity could be observed due to less charge carrier recombination and similarly reported in previous works [39]. For example, the PL intensity of g-C_3N_4 was weekend when coupled with Ti_3C_2 MXene due to preventing charge recombination [40]. This proves that V_2AlC is a good mediator to trap electrons, so the V_2AlC/g-CN composite has less recombination.

The UV–vis diffuse reflectance absorbance spectra of the materials were further conducted to understand light absorption characteristics as presented in Fig. 6(b-c). Using pure V_2AlC, no specific absorption spectrum was obtained, probably due to its conducting characteristics. For the case of g-CN, an apparent absorption spectrum within the UV–visible domain was obtained. However, high peak intensity was noticed in the UV-region, which reflects higher UV-light absorption. Additionally, when V_2AlC was coupled to layered g-CN nanosheets, the light absorption intensity in both the UV and visible regions was increased. This was probably due to the high light absorption characteristics of V_2AlC due to its dark color [41]. Previously, higher visible light absorption of Ti_3C_2 has been reported. When Ti_3C_2 was coupled with g-C_3N_4, light absorption capacity was further increased [10]. All these findings confirm that V_2AlC is favorable to improving g-C_3N_4 light absorption characteristics. The band gap energy of g-C_3N_4 and V_2AlC/g-C_3N_4 was estimated to be 2.85 eV and 2.81 eV, respectively. The VB of g-C_3N_4 was estimated in our previous work using XPS wide spectra and the value found was + 1.52 eV. Using E_{bg} and VB from the XPS wide spectrum, the conduction band (CB) position of g-C_3N_4 was calculated to be − 1.33 eV and similar observations have been reported for the VB and CB positions of g-C_3N_4 [42].

3.2. Photocatalytic CO_2 reduction

Initially, blank photocatalytic runs were performed to confirm the quality and reliability of the products with different types of photocatalytic systems. For this purpose, four sets of experiments were conducted, including (1) a photocatalyst with light source under inert gas without feed mixture; (2) a photocatalyst with feed mixture but without light source; (3) a photocatalyst with light source without feed mixture in a monolith reactor; and (4) a photocatalyst with feed mixture but without light source in a monolith

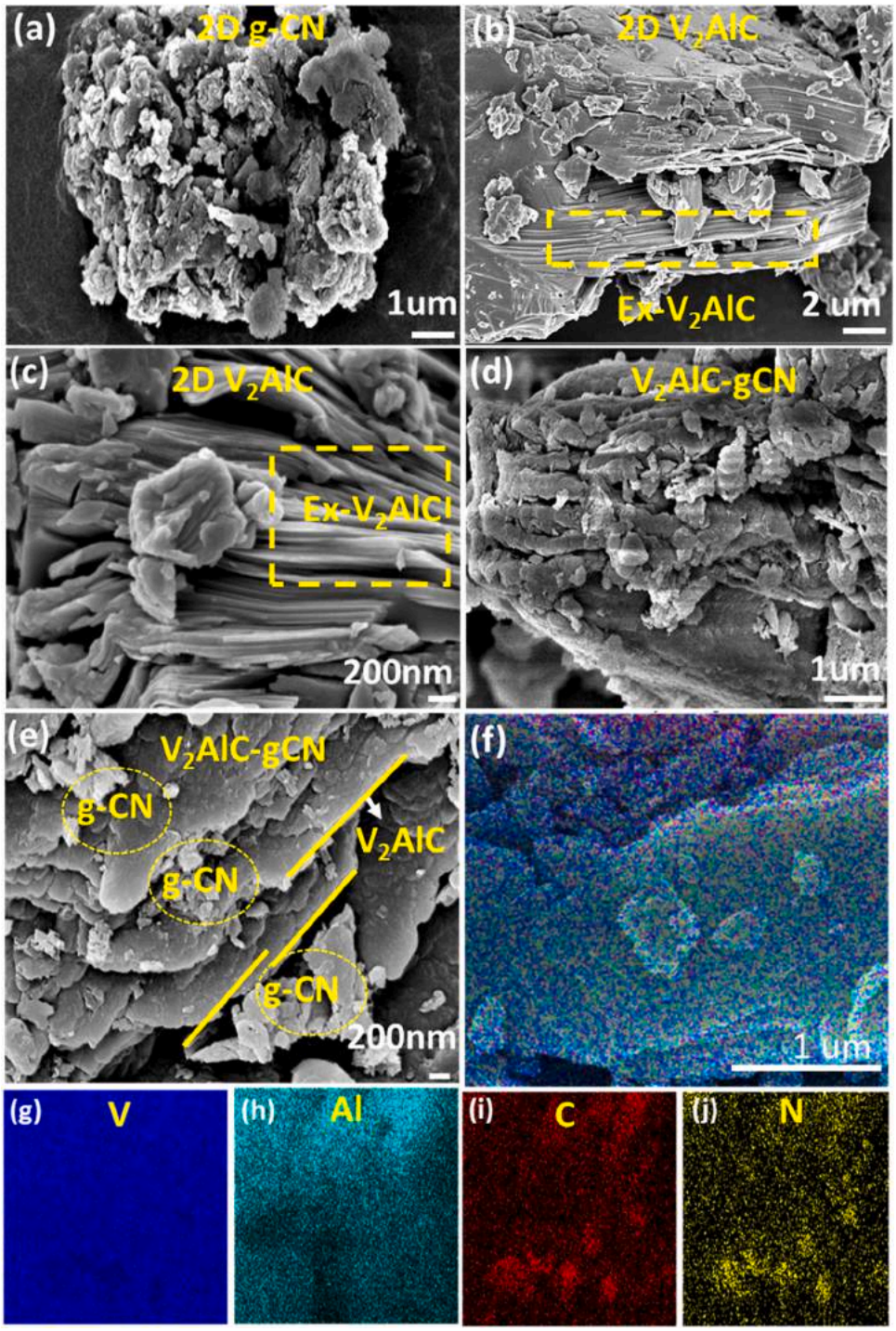

Fig. 3. FESEM analysis for; (a) g-C_3N_4, (b-c) V_2AlC, (d-e) V_2AlC loaded g-C_3N_4 samples, (f) EDX analysis for the composite V_2AlC/g-C_3N_4, (g-j) identification of V, Al, C and N elements.

photoreactor. In all these experiments, no carbon products were observed either in the absence of a light source or a feed mixture. This confirms that both the photocatalyst and photoreactor were clean and CO and CH_4 originated only during the CO_2 reduction process under light irradiation.

3.2.1. *Effect of V_2AlC loading*

The performance of V_2AlC MAX loaded g-CN was tested for photocatalytic CO_2 reduction with H_2O in a fixed bed photoreactor under UV-light irradiation. The effect of V_2AlC loading into g-CN was tested by varying different amounts of MAX, and the results for CO and CH_4 production are shown in Fig. 7. Fig. 7(a) displays CO_2 conversion to CO over several V_2AlC-loaded g-CN photocatalysts. Using pristine g-C_3N_4, CO production of 423 μmol $g^{-1}h^{-1}$ was gained. When 5% V_2AlC was dispersed with g-C_3N_4, the CO yield increased to 1073 μmol g^{-1} h^{-1}, the highest amount of 1747 μmol $g^{-1}h^{-1}$ was attained with optimized 10% V_2AlC loading. This augmented CO production during CO_2 reduction was evidently due to proficient separation of charges with a higher sorption process using layered MAX phase [39]. Previously, MAX/g-C_3N_4 was tested for photocatalytic dry reforming of methane and reported significantly enhanced photoactivity due to hindered charge carrier recombination

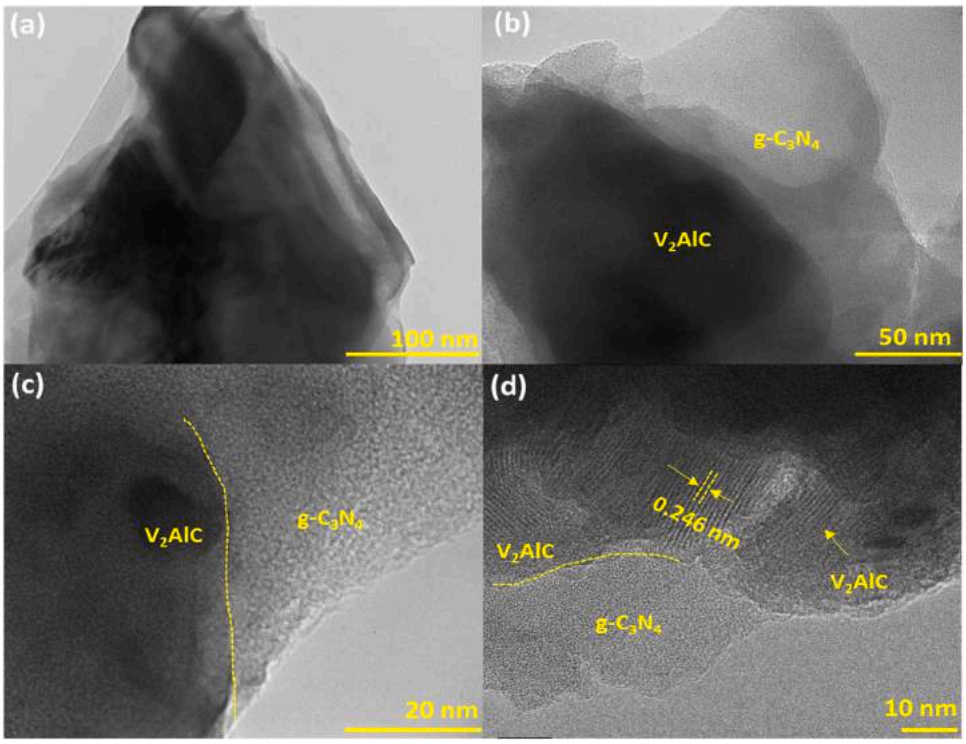

Fig. 4. TEM analysis of (a) V_2AlC, (b-c) TEM images V_2AlC loaded g-C_3N_4, (d) ᴅ-spacing analysis of V_2AlC/g-C_3N_4.

[33]. However, a decline in CO production with excessive MAX loading was undoubtedly due to generating charge recombination centers. Perhaps, it could also be due to reducing the amount of g-C_3N_4 surface available as a photocatalyst.

Fig. 7(b) shows photocatalytic CH_4 evolution during CO_2 photoreduction with H_2O over various V_2AlC-loaded g-CN samples. Using pure g-CN, a small amount of CH_4 (69 μmol g^{-1}) was attained but increased to 101 and 134 μmol g^{-1} with 5% and 10% V_2AlC-loading was employed. This obvious improved performance of the composite photocatalysts for CH_4 formation was clearly due to separation of photo-induced charge carriers in the presence of MAX as a cocatalyst. However, the decline in CH_4 production at higher MAX loading was probably because of g-CN surface coverage with MAX, thus, providing less surface area for the photocatalysis process. More importantly, CO selectivity (Fig. 7b) was improved after V_2AlC loading to g-CN. All these discoveries confirm that the 10 V_2AlC/g-CN composite is helpful for selective and dynamic CO_2 photoreduction to CO in the presence of water as the reducing agent under UV light.

The performance of V_2AlC/g-CN composite was further associated with the previously published literature. When it was tested for photocatalytic CO_2 reduction [18], the biomass derived carbon loaded g-C_3N_4 that was doped with Ag showed a CO yield rate of 33.3 μmol $g^{-1}h^{-1}$. Over 2D porous g-C_3N_4 coupled 3D TiO_2 micro flowers, enhanced CO_2 to CO/CH_4 was observed [43]. The boosted photogenerated electron-hole separation and large surface were responsible for this enhancement in photoactivity. In another work, 2D Ti_3C_2 supported $BiOIO_3$/g-C_3N_4 was tested for CO_2 photoreduction under visible light and CO and CH_4 yield rates of 5.88 and 1.55 μmol $g^{-1}h^{-1}$, respectively, were achieved. The modified Ti_3C_2 was principally responsible for boosting CO_2 photoreduction efficiency [21]. Comparatively, in the current study, the significant enhanced CO and CH_4 yield rates were obviously attributable to superior V_2AlC characteristics for charge carrier separation with high light absorption.

3.2.2. Effect of light source

The light source has a significant effect on photocatalyst performance and also on the products' selectivity [44,45]. Thus, optimized 10 V_2AlC/g-CN nanocomposite effectiveness was further explored for photocatalytic CO_2 reduction with H_2O in a fixed bed reactor under UV and visible light irradiation. The UV-light source used was a 200 W Hg lamp with a light intensity of 100 mW cm^{-2} and a wavelength of 254 nm. Similarly, for the visible light source, a 300 W Xenon lamp with the same intensity of 100 mW cm^{-2} and a wavelength of ~ 420 nm was employed. In both the light sources, CO and CH_4 were the potential products' but with different yield rates, as shown in Fig. 8(a). Using a UV-light source, a CO yield of 3495 μmol g^{-1} was produced, and this is 7.5-fold higher than its production under visible light (469 μmol g^{-1}). Similarly, the yield of CH_4 evolution under UV-light was 134 μmol g^{-1} ~ 2.5-fold extra than employing visible light irradiation. This reveals that the light source has a significant impact on the yield rate under the identical operating conditions.

Although g-C_3N_4 is functional under UV–visible light irradiation and coupling V_2AlC with g-CN, visible light absorption was increased. However, experimental results contradict this hypothesis of higher light absorption with photocatalytic performance. The effect of UV/visible light on reducing CO_2 using a fixed-bed can be explained based on different possible reasons. The first hypothesis is that UV light has more penetration depth compared to visible light irradiation. In this study, UV-light of wavelength 254 nm and visible light of 420 nm were employed and lamps were fixed at the top surface of the fixed bed reactor. Due to using a 10 mm thick glass window and a fixed bed reactor of a total length of 8 cm, there was long travelling distance for the light to travel before the photoactivation process as shown in Fig. 8(b). Thus, UV-light effectively reached to the photocatalyst surface with its more penetration depth inside the bed as well, resulting in more production of photoinduced charge carriers. On the other hand, the second possible reason can be explained of more production of charges at lower light wavelengths. As g-C_3N_4 is photoactive under both light irradiations, however,

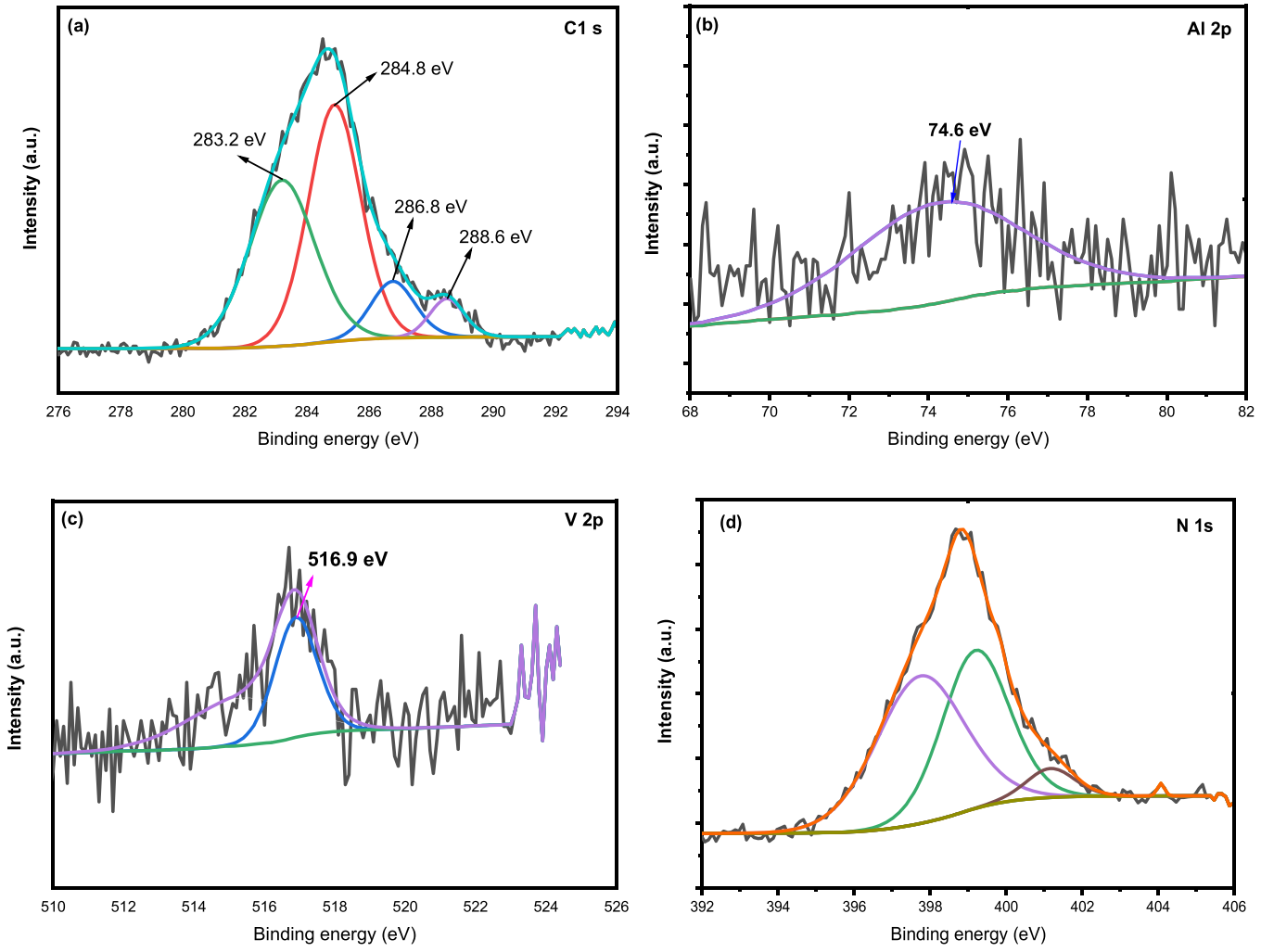

Fig. 5. XPS analysis of $V_2AlC/g\text{-}C_3N_4$ composite: (a) C 1 s, (b) Al 2p, (c) V 2p, and (d) N 1 s.

more charges would be produced using a shorter wavelength, resulting in enhanced photocatalytic efficiency. However, further investigations are recommended to scientifically justify such types of observations and experimental results. Earlier, the performance of $ZnV_2O_6/g\text{-}C_3N_4$/RGO nanocomposite was explored for the production of CO/CH_4 during CO_2 reduction under UV/visible light irradiation [46]. The higher number of products was obtained under UV-light irradiation because of abundant electron creation in relation of higher light penetration depth.

3.2.3. *Effect of sacrificial reagent*

The performance of the $V_2AlC/g\text{-}C_3N_4$ composite photocatalyst was further conducted using different sacrificial sources, namely methanol and hydrogen, with fixed-bed photoreactor under UV-light. To investigate the effect of methanol, initially, a 5 vol% methanol solution with water was prepared for saturating CO_2 gas with methanol-water vapors. Similarly, hydrogen sources were used to carry the reaction with CO_2, regulated by MFC with a CO_2/H_2 feed ratio of 1.0. The CO yield during CO_2 photoreduction with different sacrificing reagents is shown in Fig. 9(a). Obviously, different amounts of CO were obtained with water, methanol and hydrogen sacrificial reagents. Using CO_2-H_2O, initially, higher amount of CO was obtained. However, its production was lower than CO_2-CH_3OH with time on irradiation until it reached 60 min. This reveals, that methanol is a promising sacrificial reagent to promote CO_2 reduction to CO over the $V_2AlC/g\text{-}C_3N_4$ composite. Unexpectedly, the lowest CO production was obtained with hydrogen introduced. The performance of the $V_2AlC/g\text{-}C_3N_4$ composite for CH_4 evolution during CO_2 photoreduction with H_2O, methanol, and hydrogen is demonstrated in Fig. 9(b). The results for CH_4 production were entirely different than for CO production with water and methanol as the sacrificial reagents. Using CO_2-water, highest CH_4 was formed. In the case of the CO_2-CH_3OH feed mixture, the production of CH_4 was much closer to the amount of CH_4 produced, while using water as the sacrificial reagent. In general, in all these systems, the production of methane was not significant.

It is evident from the above discussion that the CO was the major CO_2 reduction product over the $V_2AlC/g\text{-}C_3N_4$ composite photocatalyst with a smaller amount of CH_4 formation. Using CH_3OH and H_2 as the sacrificial reagent, the selectivity of CO was not much altered, whereas its yield was somewhat varied with the sacrificial reagent. All these findings can be explained based on the different possibilities. The adsorption of water and methanol over the $V_2AlC/g\text{-}C_3N_4$ composite would be more proficient compared to hydrogen due to specific surface functional group of $g\text{-}C_3N_4$. This enables more attachment of H_2O and CH_3OH over the $g\text{-}C_3N_4$ surface, enabling effectual CO_2 photoreduction. In addition, higher CO production with CO_2-CH_3OH was due to increasing number of protons (H^+) with alcohol in the feed mixture. Previously, we investigated photocatalytic water splitting with methanol as the sacrificial reagent and noticed a significant amount of H_2 and CH_4 production under UV light irradiation [47]. In another development, we observed higher

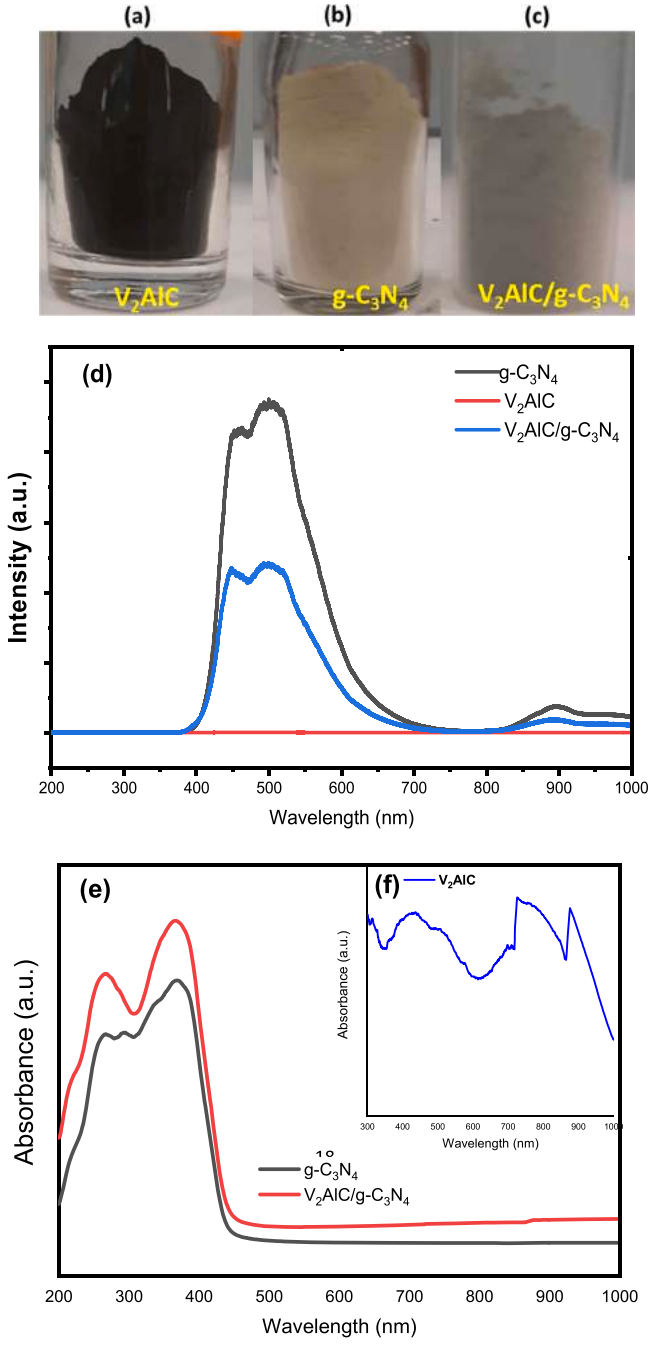

Fig. 6. (a) Image of V_2AlC, (b) image of g-C_3N_4, (c) image of V_2AlC/g-C_3N_4, (d) PL spectra of g-C_3N_4 and V_2AlC loaded g-C_3N_4 samples, (e-f) UV–visible diffuse reflectance spectra of g-C_3N_4, V_2AlC and V_2AlC/g-C_3N_4 composite samples.

production of H_2 over Ti_3C_2/g-C_3N_4 composite using methanol as the sacrificial reagent compared to glycerol. Comparatively, in another work, we observed higher hydrogen production over TiO_2 using glycerol as the sacrificial reagent compared to methanol [48]. This reveals that methanol has more attachment with g-C_3N_4, using monolithic support, there was an efficient reforming reaction, enabling more availability of protons for the reduction of CO_2 under UV-light irradiation.

Formerly, we examined the performance of Ti_3C_2/g-C_3N_4 with in-situ grown TiO_2 for CO_2 reduction with the involvement of CH_3OH, water, and H_2. It was noticed that CO_2-H_2O was favorable for CO production, whereas, a higher amount of CH_4 was obtained in the presence of methanol [42]. This contradiction in results was possibly

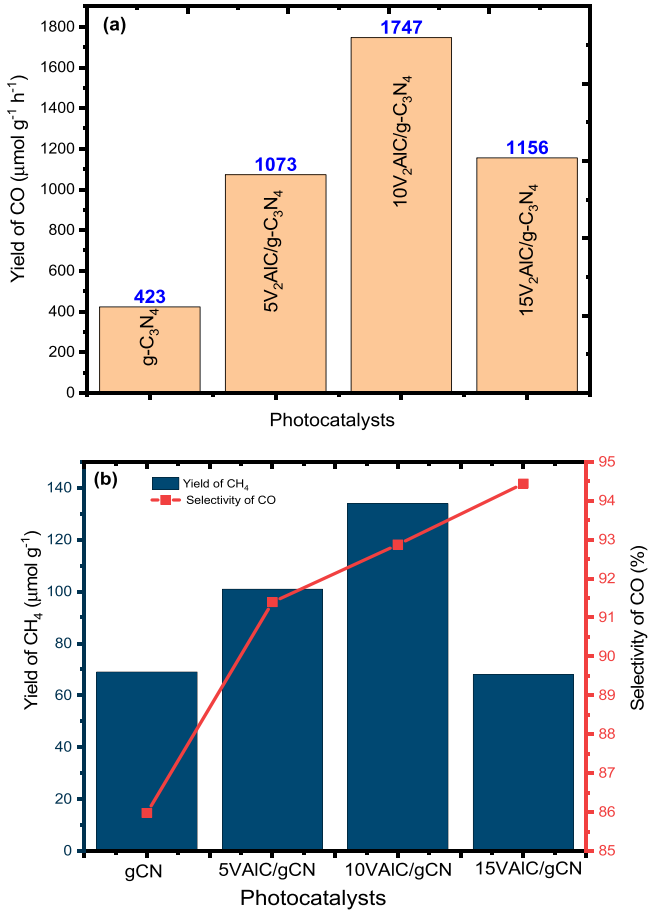

Fig. 7. Effect of V_2AlC MAX loading on the performance of g-CN for photocatalytic CO_2 reduction with H_2O in a fixed bed photoreactor under UV-light irradiation; (a) CO production, (b) CH_4 production and CO selectivity.

due to the presence of TiO_2 NPs and because of Ti_3C_2 MXene instead of V_2AlC MAX.

3.2.4. Performance evaluation of fixed-bed and monolith photoreactor

The photocatalysis process is also purposely dependent on the types and operations of photocatalytic reactor systems [44]. Therefore, in this study, a fixed bed and a monolith photoreactors operated in a batch mode was selected to further investigate the V_2AlC/g-C_3N_4 composite photocatalyst performance. The photocatalytic reduction of CO_2 to CO with CH_3OH as the sacrificial reagent while using fixed bed and monolith photoreactors is discussed in Fig. 10(a). Comparatively, more CO was produced with a monolith reactor compared with the fixed-bed while keeping all the parameters identical. Similarly, a higher CH_4 was produced using a monolith reactor during CO_2 reduction with a methanol-water mixture. This was evidently due to higher distribution of light over the monolithic surface with more mass transfer and reaction kinetics with monolith microchannels. Earlier, we looked at the performance of a fixed-bed and monolith photoreactors. We found that that CO and CH_4 production was much higher in a monolith photoreactor because there was minimum mass transfer limitation and more illuminated active surface area available for the reaction [49].

Furthermore, the performance of the monolith photoreactor was conducted using water and methanol as the sacrificial reagents, as demonstrated in Fig. 10(b). Using CO_2-methanol, the most CH_4 was produced at the start of the reaction; however, it gradually reached a steady state with time on stream. However, unceasing CO evolution was observed using both reducing agents. During CO_2 reduction by H_2O, CO was produced in a significant amount; however, CO_2-

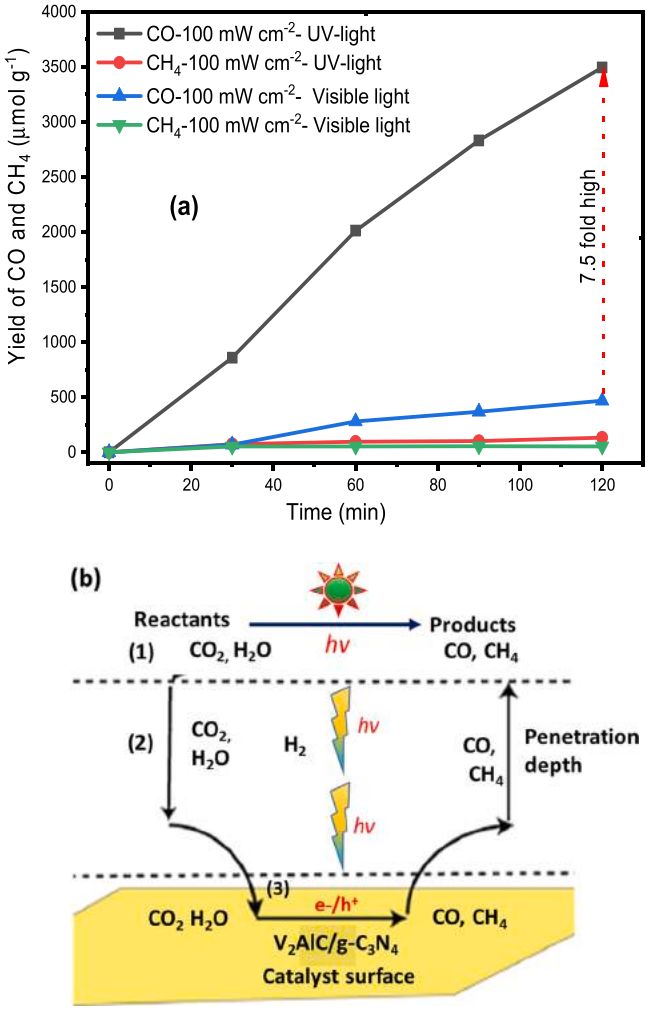

Fig. 8. (a) Performance analysis of 10 V_2AlC/g-CN composite for CO_2 photoreduction by H_2O under UV/visible light for the production of CO and CH_4 in a fixed bed photoreactor; (b) Schematic illustration of light penetration depth and surface reactions.

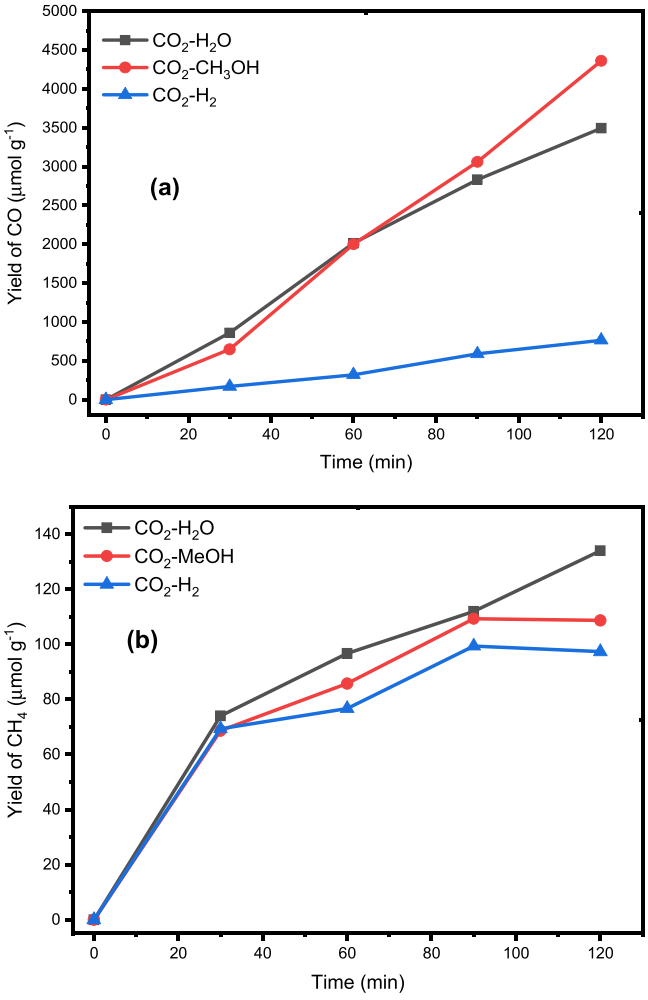

Fig. 9. Effect of methanol and hydrogen sacrificial reagent on the performance of V_2AlC/g-C_3N_4 for photocatalytic CO_2 reduction under UV-light in a fixed bed photoreactor; (a) CO production; (b) CH_4 production.

methanol was favorable for more methane formation. Comparatively, CO consumed 2 electrons compared to 8 electrons for CH_4 formation. Furthermore, in a monolith photoreactor, reversed water gas shift reaction is favorable. Thus, initially, more CO would be produced due to more production of protons, and some of the CO would be converted back to CO_2, resulting in lower CO formation. These observations can be explained based on the different hypotheses and light penetration depth as discussed in Fig. 9(c). Using a CO_2-water system, a lower amount of H^+ was produced, which was effectively consumed for CO production. On the other hand, using methanol, there is more possible generation of electrons and protons (H^+) that are required for CH_4 formation.

Previously, CO_2 photoreduction with H_2O was examined in a cylindrical fixed-bed and monolith photoreactor and observed more CH_4 evolution with the fixed-bed than with the monolith photoreactor, which is helpful for CO formation [49]. Similarly, substantial CH_4 evolution over Ti_3AlC_2/TiO_2 composite photocatalyst was observed due to promising charge carrier separation [27]. On the other hand, a monolith photoreactor system with Ni-MMT loaded TiO_2 was helpful for selective CO production during reduction of CO_2 under UV-light [32]. This reveals promising performance of a monolithic system for selective CO formation. However, fixed bed photoreactor selectivity is greatly depends on the photocatalyst under observation.

The performance of the current work was further compared with the previous research, and the results are summarized in Table 1. Clearly, there is an increase in research on photocatalytic CO_2 reduction; however, in majority of works, CO has been reported as the main product. For example, the NiAl-LDH/g-C_3N_4/GA composite was tested for photocatalytic CO_2 reduction and CO as the main product with yield rate of 28.83 µmol^{-1} h^{-1} was reported [50]. Similarly, in another development, a $Ti_3C_2/BiOIO_3$/g-C_3N_4 composite was tested under visible light irradiation and a CO yield rate of 5.88 µmol^{-1} h^{-1} was achieved during the CO_2 reduction process. All these findings confirm the higher yield rate of CO and CH_4 over the V_2AlC/g-C_3N_4 composite due to the efficient design of the photoreactor and the proficient separation of charge carriers due to the presence of V_2AlC MAX.

3.3. Stability analysis

The stability and recyclability tests are imperative to estimate the photocatalyst's appropriateness for commercial acceptance. For this drive, the assessment of the V_2AlC/g-C_3N_4 composite was conducted in multiple cycles for photocatalytic reduction of CO_2 with a methanol-water mixture in a fixed bed system. After every completed cycle, the lamp was turned off and products from the reactor were cleaned with feed gases before starting the next cycle. Fig. 11(a) shows the performance of the composite photocatalyst for the production of CO and CH_4 in consecutive four cycles. Evidently,

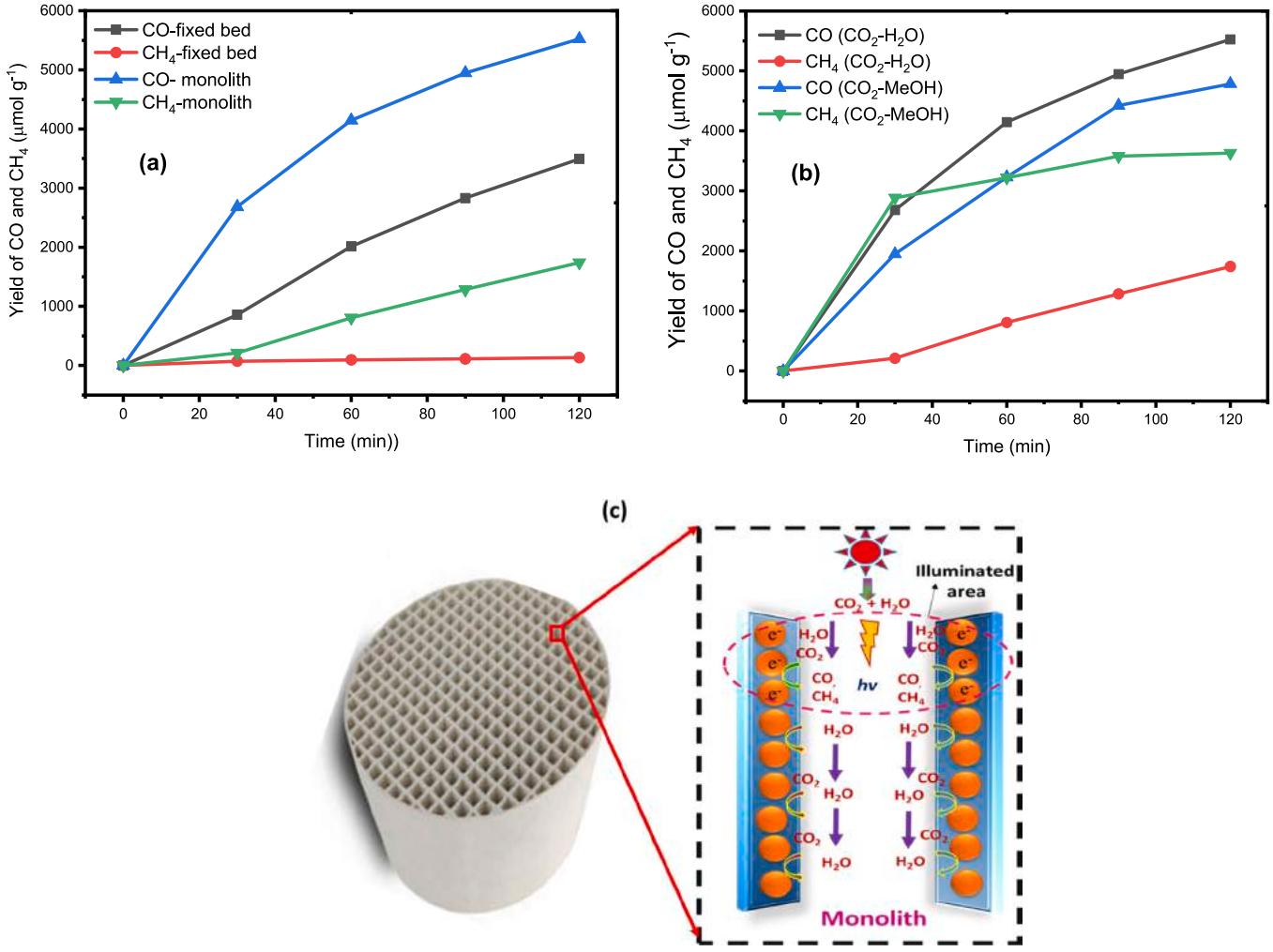

Fig. 10. (a) Performance comparison between fixed-bed and monolith photoreactors for photocatalytic reduction of CO_2 by H_2O under UV-light; (b) Results of sacrificial reagent for photocatalytic reduction of CO_2 using monolith photoreactor; (c) Schematic illustration of single channel monolith for light and mass transfer process.

Table 1
Performance comparison of $V_2AlC/g\text{-}C_3N_4$ with previous various literature for photocatalytic CO_2 reduction over various photocatalysts.

Photocatalyst	Parameters/Reactor	Light source	Yield rate (μmol g^{-1} h^{-1})	Ref.
$V_2AlC/g\text{-}C_3N_4$	Fixed bed, CO_2-H_2O	200 W Hg lamp	CO= 1747 CH_4 = 67	Current work
$V_2AlC/g\text{-}C_3N_4$	Monolith reactor, CO_2-H_2O	200 W Hg lamp	CO= 2765 CH_4 = 871.5	Current work
NiAl-LDH/g-C_3N_4/GA	CO_2-water vapour	300 W Xe lamp	CO= 28.83	[50]
GQDs/Bi_2WO_6	200 mL Lab solar Reactor, 90 mL of DI water and 10 mL TEA,	300 W Xe lamp	CO= 43.9	[51]
NH_2-UiO-66/SiC	200 mL quartz reactor	300 W Xe lamp	CO= 7.3 CH_4 = 0.26	[52]
Ag-Cu_2O/TiO_2	CO_2-water vapour, surface coated catalyst	300 Xenon lamp, AM 1.5 G filter,	CO= 13.19 CH_4 = 1.74	[2]
Ti_3AlC_2/g-C_3N_4/TiO_2	Fixed bed, CO_2-H_2O	35 W HID lamp	CH_4 = 2103.5 CO= 297.26	[49]
Ti_3AlC_2/g-C_3N_4/TiO_2	Monolith reactor, CO_2-H_2O	300 W Xenon lamp	CO= 1510.44 CH_4 = 139.77	[49]
$LaCoO_3$/g-C_3N_4	Fixed bed, CO_2-H_2O	35 W HID lamp	CO= 33.85 CH_4 = 12.13	[53]
CoAlLa-LDH/g-C_3N_4	Fixed bed, CO_2-H_2O	35 W HID lamp	CO= 17.85 CH_4 = 14.66	[54]
$Ti_3C_2/BiOIO_3$/g-C_3N_4	CO_2-H_2O	Simulated sunlight	CO= 5.88 CH_4 = 1.55	[21]

continuous CO and CH_4 evolution rates were observed over the entire irradiation using $V_2AlC/g\text{-}C_3N_4$ composite. The trends for CO and CH_4 production were consistent for four cycles. This reveals the higher stability of g-C_3N_4 with V_2AlC MAX for continuous CO and CH_4 generation during CO_2 photoreduction. More importantly, the somewhat increased CO production was observed after every cycle. This could probably due to intermediate carbon materials being reacted with oxygen and converted to CO during photocatalysis

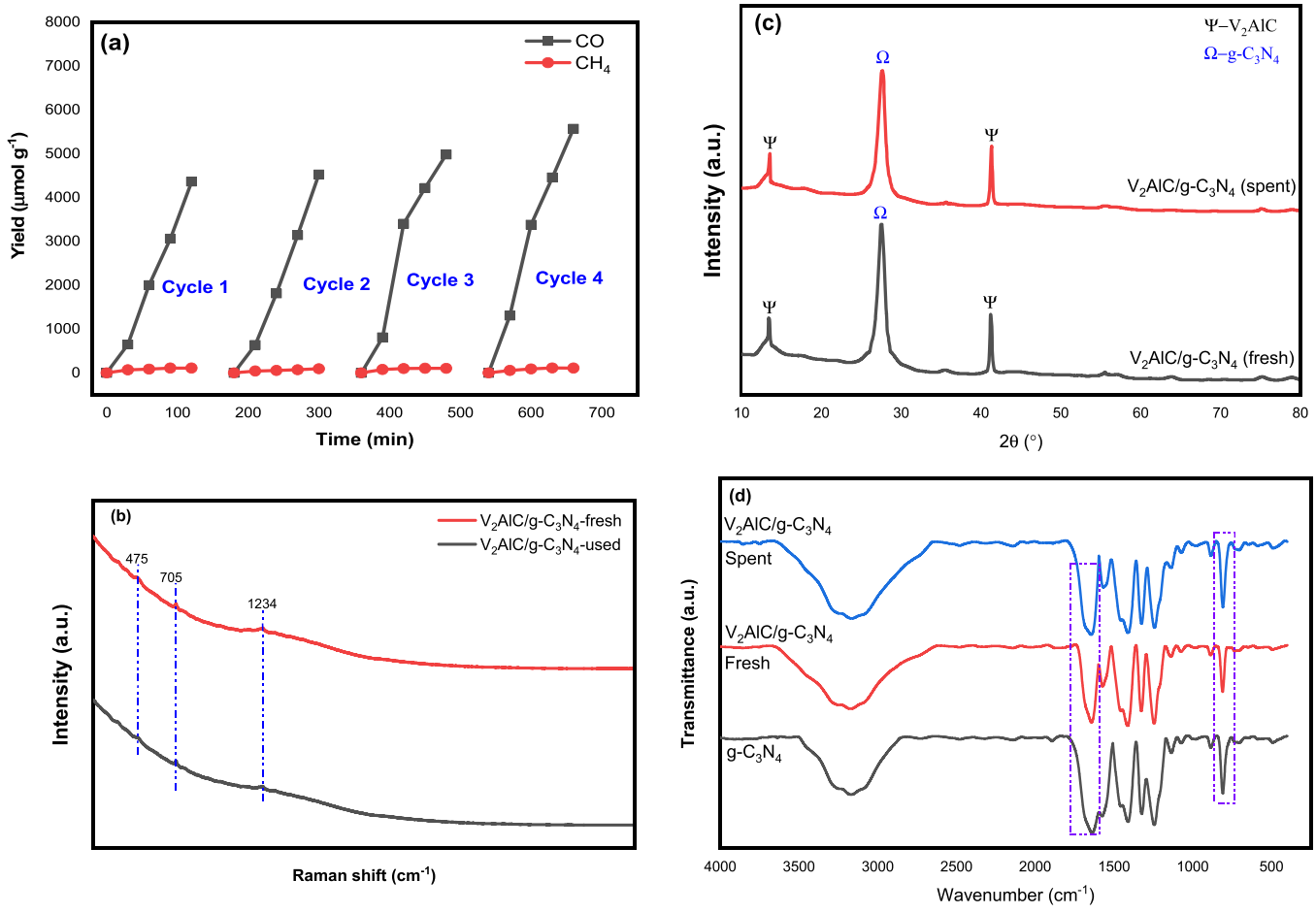

Fig. 11. (a) Stability plots for CO and CH_4 evolution using $V_2AlC/g\text{-}C_3N_4$ for photocatalytic conversion of CO_2 with fixed-bed photoreactor; (b) Raman spectra of fresh and spent $V_2AlC/g\text{-}C_3N_4$ composite photocatalyst; (c) XRD analysis of fresh and spent $V_2AlC/g\text{-}C_3N_4$; (d) FTIR analysis of fresh and spent $V_2AlC/g\text{-}C_3N_4$ composite samples.

process. Previously, 2D/2D Ti_3C_2 supported $g\text{-}C_3N_4$ has been tested for photocatalytic CO and CH_4 production during the CO_2 reduction and reported increased and decreased stability during multiple cycles of testing [40].

To further confirm the stability of the $V_2AlC/g\text{-}C_3N_4$ composite photocatalyst, Raman plots of both the fresh and spent samples are presented in Fig. 11(b). Apparently, identical Raman peaks were observed. This reveals that the composite photocatalyst was very stable and there was no alternation in peak position even after four cycles. Furthermore, spent $V_2AlC/g\text{-}C_3N_4$ was further characterized using XRD and the results are shown in Fig. 11(c). Both fresh and spent catalysts have identical peaks and any additional peaks were not identified, which confirms that the spent catalyst is pure and the composite was not oxidized or its structure was not changed. Fig. 11(d) shows FTIR analysis of $g\text{-}C_3N_4$, $V_2AlC/g\text{-}C_3N_4$ and spent $V_2AlC/g\text{-}C_3N_4$ samples. For the pristine $g\text{-}C_3N_4$ sample, the broad peaks in the range of 3000–3500 cm^{-1} are attributed to N-H stretching vibration of amino groups and the O-H vibration due to adsorbed over the surface. The obvious peak at 1636 cm^{-1} corresponds to stretching vibration of C-N, whereas four peaks between 1500 and 1400 cm^{-1} belong to aromatic CN stretching vibration. Finally, the peak at 808 cm^{-1} is attributed to breathing mode of triazine units [35,36]. All the characteristic peaks of $g\text{-}C_3N_4$ can be obviously found in the V_2AlC loaded $g\text{-}C_3N_4$ composite, confirming the intact structure of $g\text{-}C_3N_4$ in the composite and findings are in good agreement with Raman and XRD results. More importantly, fresh and spent $V_2AlC/g\text{-}C_3N_4$ composite samples have similar peak positions, confirming no change in peak position. Besides, additional peaks were not identified in the spent composite sample, which further confirmed the high stability of the sample without any change in structure.

Obviously, all the characterizations, including Raman, XRD, and FTIR, analysis confirm that samples have identical band positions and additional peaks were not identified, which confirms that the spent catalyst composition is not changed. However, an increase in CO production during multiple cyclic runs would be due to more interaction between the elements and because of some organic residues, which are responsible for more CO production. Previously, we investigated $WO_3/g\text{-}C_3N_4$ for photocatalytic CO_2 reduction to CO and CH_4 and observed an increase in CO production in multiple cycles due to partial oxidation of the composite or because of adsorbed intermediate species converted to CO during multiple cycles [55]. Using a monolith photoreactor loaded with the Ni-MMT/TiO_2, obvious increment in H_2 evolution was detected during CO_2 reduction to CO and CH_4 under UV-light irradiation [32]. In another development, increased in CO production was observed in multiple cycles using a monolith photoreactor dispersed with Fe-clay/TiO_2 catalyst under UV-light irradiation [31]. In several other works, an increase in CO production in multiple cycles in the presence of monolith photoreactor has been reported [56]. All these findings support the present results; however, further investigations are required to understand the mechanics of such an increment in productivity in multiple cycles.

Previously, in various papers, photostability in cyclic runs for photocatalytic reduction of CO_2 has been investigated. For example, 2D Ti_3C_2 was anchored over $g\text{-}C_3N_4$ as a cocatalyst and observed to somewhat decline in photoactivity for CH_4 production in multiple cycles. The physicochemical properties of the spent composite were

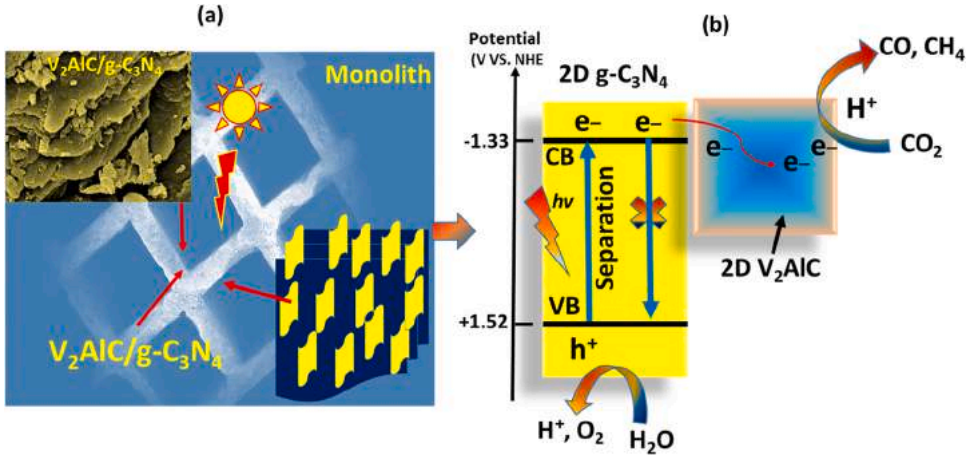

Fig. 12. Schematic illustration for photocatalytic CO_2 reduction with H_2O over $V_2AlC/g\text{-}C_3N_4$ for the production of CO and CH_4.

analyzed using XRD, FTIR, and SEM, and no changes in morphology and structure were discovered [10]. Similarly, a declined in photoactivity in multiple cycles was observed when $NiO/g\text{-}C_3N_4$ was tested for photocatalytic CO_2 reduction to CO/CH_4 [9]. In general, a highly stable and effective V_2AlC/gC_3N_4 composite was found, which was beneficial for continuous CO and CH_4 production under all types of operating conditions.

3.4. Proposed reaction mechanism for CO_2 reduction

In photocatalysis, understanding reaction pathways is essential for promoting photocatalytic activity. As discussed, earlier, during CO_2 reduction with water and other sacrificial reagents, CO was observed as a potential product with considerable CH_4 production. The mechanism for CO_2 photoreduction with $V_2AlC/g\text{-}C_3N_4$ for the production of CO and CH_4 with fixed-bed and monolith photoreactor has been discussed in Fig. 12. When a catalyst is immobilized as thin film over the monolith surface, it provides a more illuminated active surface, allowing for more production of photoinduced charge carriers, as depicted in Fig. 12(a). The photogenerated charges over the $g\text{-}C_3N_4$ surface under light irradiation has potential to recombine due to their short lifetime. However, due to 2D/2D heterojunction construction between $g\text{-}C_3N_4$ and V_2AlC, there is a good interfacial coupling for separating photoinduced charges with their minimum recombination as portrayed in Fig. 12(b).

Using V_2AlC as the cocatalyst, higher separation of charges with their minimum recombination over the $g\text{-}C_3N_4$ surface was achieved due to higher electrical conductivity of MAX-based materials [57,58]. In a recent development, it has been reported that a suitable fermi level of V_2C with TiO_2, enabling proficient electron transfer within the interface [59]. Similarly, V_2AlC would also be promising to trap and transport electrons from $g\text{-}C_3N_4$ due to good interface interaction. The photogenerated holes would be used to oxidize water (Eq. 1), whereas, electrons accumulated over MAX surface would be consumed by CO_2 to produce CO and CH_4 as illustrated in Eqs. (2–4) [2,60].

$$H_2O + 2h^+ \rightarrow \frac{1}{2}O_2 + 2H^+ \qquad (1.23\ eV\ vs\ NHE) \tag{1}$$

$$CO_2 + e^- \rightarrow \cdot CO_2^- \tag{2}$$

$$CO_2 + 2H^+ + 2e^- \rightarrow CO + H_2O \qquad (-0.48 eV vs NHE) \tag{3}$$

$$CO_2 + 8H^+ + 8e^- \rightarrow CH_4 + 2H_2O \qquad (-0.24 eV vs NHE) \tag{4}$$

Due to good interface interaction and the higher reduction potential of $g\text{-}C_3N_4$, production of CO was increased in significant amount compared to CH_4. This is obvious because CO requires two electrons compared with 8 electrons for CH_4 evolution. In addition, the conduction band of $g\text{-}C_3N_4$ (−1.33 eV) is more negative than the CO_2/CO reduction potential (−0.50 eV). Thus, the production of CO is a favorable process over the composite photocatalyst. In addition, the higher amount of CO evolution over V_2AlC/gC_3N_4 was due to additional generating and separating charge carriers under UV-light [61]. When monolith photoreactor was used, performance of $V_2AlC/g\text{-}C_3N_4$ was further increased due to the more light irradiation available for the production of electrons and because of more illuminated active surface of the monolithic surface.

4. Conclusions

The well-designed $V_2AlC/g\text{-}C_3N_4$ was effectively synthesized and its photoactivity was tested for CO_2 photoreduction under UV and visible light in a stainless steel fixed-bed and a monolith reactor. Using V_2AlC coupled g-CN nanotexture, CO and CH_4 as the main products were obtained under both types of lights sources and photoreactors. Under UV-light irradiation, the efficiency of $V_2AlC/g\text{-}C_3N_4$ composite was 4.13 folds higher than using$g\text{-}C_3N_4$, which was clearly because of efficient separation of charges by V_2AlC MAX as the electron mediator. Furthermore, comparing light sources, higher CO and CH_4 amounts were obtained using UV-light irradiation due to more light penetration depth with more electron generation. Similarly, among the sacrificial reagents such as H_2O, CH_3OH, and H_2, highest CO yield was obtained with methanol as the sacrificial reagent due to additional charge generation. More interestingly, the monolith photoreactor was found promising to stimulate CO yield due to its more illuminated active surface compared to the fixed-bed photoreactor. On the other hand, CO_2-water was more favorable for CO evolution, whereas CO_2-methanol was more beneficial for CH_4 evolution in a monolith photoreactor. All these findings confirm the higher performance and stability of the $V_2AlC/g\text{-}CN$ composite and would also be valuable for other photocatalytic energy and environmental applications.

CRediT authorship contribution statement

Beenish Tahir: Methodology, Writing – original draft, Reactions performance and material characterizations. **Muhammad Tahir:** Conceptualization, Data curation, Formal analysis, Funding acquisition, Writing – review & editing. **Mohd Ghazali Mohd Nawawai:** Supervision, Research management.

Data Availability

No data was used for the research described in the article.

Declaration of Competing Interest

The authors declare that they have no known competing financial interests or personal relationships that could have appeared to influence the work reported in this paper.

Acknowledgements

The authors would like to extend their appreciation to United Arab Emirates University (UAEU), United Arab Emirates (UAE) for the financial support of this research under Startup Research Grant (vote no.12N097).

References

[1] L. Zhang, F. Wang, J. Zhu, B. Han, W. Fan, L. Zhao, W. Cai, Z. Li, L. Xu, H. Yu, W. Shi, CO_2 reforming with methane reaction over Ni@SiO_2 catalysts coupled by size effect and metal-support interaction, Fuel 256 (2019) 115954.
[2] X. Wang, Z. Jiang, H. Chen, K. Wang, X. Wang, Photocatalytic CO_2 reduction with water vapor to CO and CH_4 in a recirculation reactor by Ag-Cu_2O/TiO_2 Z-scheme heterostructures, J. Alloy. Compd. 896 (2022) 163030.
[3] H. Wang, S. Cheng, X. Cai, L. Cheng, R. Zhou, T. Hou, Y. Li, Photocatalytic CO_2 reduction to HCOOH over core-shell Cu@Cu_2O catalysts, Catal. Commun. 162 (2022) 106372.
[4] W. Ma, M. Xie, S. Xie, L. Wei, Y. Cai, Q. Zhang, Y. Wang, Nickel and indium core-shell co-catalysts loaded silicon nanowire arrays for efficient photoelectrocatalytic reduction of CO_2 to formate, J. Energy Chem. 54 (2021) 422–428.
[5] Q. Wang, L. Xiao, X. Liu, X. Sun, J. Wang, H. Du, Special Z-scheme Cu_3P/TiO_2 hetero-junction for efficient photocatalytic hydrogen evolution from water, J. Alloy. Compd. 894 (2022) 162331.
[6] L. Wang, G. Huang, L. Zhang, R. Lian, J. Huang, H. She, C. Liu, Q. Wang, Construction of TiO_2-covalent organic framework Z-Scheme hybrid through coordination bond for photocatalytic CO_2 conversion, J. Energy Chem. 64 (2022) 85–92.
[7] M.A. Ávila-López, E. Luévano-Hipólito, L.M. Torres-Martínez, Optimizing the CO_2 reduction to produce CH_3OH using flexible $NiMoO_4$ coatings as a photocatalyst, J. Alloy. Compd. 918 (2022) 165549.
[8] M. Molina-Muriel, Y. Peng, H. García, A. Ribera, Increased photocatalytic activity and selectivity towards methane of trimetallic NiTiAl-LDH, J. Alloy. Compd. 897 (2022) 163124.
[9] L. Wang, Y. Dong, J. Zhang, F. Tao, J. Xu, Construction of NiO/g-C_3N_4 p-n heterojunctions for enhanced photocatalytic CO_2 reduction, J. Solid State Chem. 308 (2022) 122878.
[10] J. Hu, J. Ding, Q. Zhong, Ultrathin 2D Ti_3C_2 MXene Co-catalyst anchored on porous g-C_3N_4 for enhanced photocatalytic CO_2 reduction under visible-light irradiation, J. Colloid Interface Sci. 582 (Pt B) (2021) 647–657.
[11] R.R. Ikreedeegh, M. Tahir, Facile fabrication of well-designed 2D/2D porous g-C_3N_4–GO nanocomposite for photocatalytic methane reforming (DRM) with CO_2 towards enhanced syngas production under visible light, Fuel 305 (2021) 121558.
[12] X. Li, J. Xiong, X. Gao, J. Huang, Z. Feng, Z. Chen, Y. Zhu, Recent advances in 3D g-C_3N_4 composite photocatalysts for photocatalytic water splitting, degradation of pollutants and CO_2 reduction, J. Alloy. Compd. 802 (2019) 196–209.
[13] L. Zeng, J.-W. Chen, L. Zhong, W. Zhen, Y.Y. Tay, S. Li, Y.-G. Wang, L. Huang, C. Xue, Synergistic effect of Ru-N_4 sites and Cu-N_3 sites in carbon nitride for highly selective photocatalytic reduction of CO_2 to methane, Appl. Catal. B 307 (2022) 121154.
[14] M. Li, Y. Wu, E. Gu, W. Song, D. Zeng, Anchoring CuO nanospindles on g-C_3N_4 nanosheets for photocatalytic pollutant degradation and CO_2 reduction, J. Alloy. Compd. 914 (2022) 165339.
[15] Q. Heng, B. Wang, X. Fan, W. Chen, X. Li, L. Mao, W. Shangguan, Enhanced photoreduction activity of CO_2 to CO over Ag-loaded mesoporous g-C_3N_4 (MCN) by promoting charge separation and CO_2 adsorption, J. Alloy. Compd. 920 (2022) 165945.
[16] P. Wang, M. Yang, S. Tang, Y. Li, X. Lin, H. Zhang, Z. Zhu, F. Chen, Z-scheme heterojunctions composed of 3D graphene aerogel/g-C_3N_4 nanosheets/porous ZnO nanospheres for the efficient photocatalytic reduction of CO_2 with H_2O under visible light irradiation, J. Alloy. Compd. 918 (2022) 165607.
[17] C. Sun, Y. Liu, Z. Wang, P. Wang, Z. Zheng, H. Cheng, X. Qin, X. Zhang, Y. Dai, B. Huang, Self-assembled g-C_3N_4 nanotubes/graphdiyne composite with enhanced photocatalytic CO_2 reduction, J. Alloy. Compd. 868 (2021) 159045.
[18] Y. Li, Z. Liu, Z. Li, Q. Wang, Renewable biomass-derived carbon-supported g-C_3N_4 doped with Ag for enhanced photocatalytic reduction of CO_2, J. Colloid Interface Sci. 606 (2) (2022) 1311–1321.
[19] F. Sarwar, M. Tahir, H. Alias, Synergistic effect of photo-reduced Ni–Ag loaded g-C_3N_4 nanosheets for efficient visible Light-Driven photocatalytic hydrogen evolution, Mater. Sci. Semicond. Process. 137 (2022) 106187.
[20] M. Arumugam, M. Tahir, P. Praserthdam, Effect of nonmetals (B, O, P, and S) doped with porous g-C_3N_4 for improved electron transfer towards photocatalytic CO_2 reduction with water into CH_4, Chemosphere 286 (Pt 2) (2021) 131765.
[21] L.-f Hong, R.-t Guo, Y. Yuan, X.-y Ji, Z.-d Lin, X.-f Yin, W.-g Pan, 2D Ti_3C_2 decorated Z-scheme $BiOIO_3$/g-C_3N_4 heterojunction for the enhanced photocatalytic CO_2 reduction activity under visible light, Colloids Surf. A 639 (2022) 128358.
[22] P. Bhavani, M. Hussain, Y.-K. Park, Recent advancements on the sustainable biochar based semiconducting materials for photocatalytic applications: a state of the art review, J. Clean. Prod. 330 (2022) 129899.
[23] Z. Wu, C. Li, Z. Li, K. Feng, M. Cai, D. Zhang, S. Wang, M. Chu, C. Zhang, J. Shen, Z. Huang, Y. Xiao, G.A. Ozin, X. Zhang, L. He, Niobium and titanium carbides (MXenes) as superior photothermal supports for CO_2 photocatalysis, ACS Nano 15 (3) (2021) 5696–5705.
[24] W. Yang, G. Ma, Y. Fu, K. Peng, H. Yang, X. Zhan, W. Yang, L. Wang, H. Hou, Rationally designed Ti_3C_2 MXene@TiO_2/$CuInS_2$ Schottky/S-scheme integrated heterojunction for enhanced photocatalytic hydrogen evolution, Chem. Eng. J. 429 (2022) 132381.
[25] S. Venkateshalu, A.N. Grace, MXenes—A new class of 2D layered materials: synthesis, properties, applications as supercapacitor electrode and beyond, Appl. Mater. Today 18 (2020) 100509.
[26] S. Zada, H. Lu, F. Yang, Y. Zhang, Y. Cheng, S. Tang, W. Wei, Y. Qiao, P. Fu, H. Dong, X. Zhang, V_2C nanosheets as dual-functional antibacterial agents, ACS Appl. Bio Mater. 4 (5) (2021) 4215–4223.
[27] M. Tahir, B. Tahir, Constructing a stable 2D/2D heterojunction of oxygen-cluster-modified Ti_3AlC_2 MAX cocatalyst with proton-rich C_3N_4 for highly efficient photocatalytic CO_2 methanation, Ind. Eng. Chem. Res. 59 (21) (2020) 9841–9857.
[28] M. Tahir, Enhanced photocatalytic CO_2 reduction to fuels through bireforming of methane over structured 3D MAX Ti_3AlC_2/TiO_2 heterojunction in a monolith photoreactor, J. CO_2 Util. 38 (2020) 99–112.
[29] V. Presser, M. Naguib, L. Chaput, A. Togo, G. Hug, M.W. Barsoum, First-order Raman scattering of the MAX phases: Ti_2AlN, $Ti_2AlC_{0.5}N_{0.5}$, Ti_2AlC, $(Ti_{0.5}V_{0.5})_2AlC$, V_2AlC, Ti_3AlC_2, and Ti_3GeC_2, J. Raman Spectrosc. 43 (1) (2012) 168–172.
[30] X. Yang, Y. Zhang, Z. Fu, Z. Lu, X. Zhang, Y. Wang, Z. Yang, R. Wu, Tailoring the electronic structure of transition metals by the V_2C MXene support: excellent oxygen reduction performance triggered by metal-support interactions, ACS Appl. Mater. Interfaces 12 (25) (2020) 28206–28216.
[31] M. Tahir, Photocatalytic carbon dioxide reduction to fuels in continuous flow monolith photoreactor using montmorillonite dispersed Fe/TiO_2 nanocatalyst, J. Clean. Prod. 170 (2018) 242–250.
[32] M. Tahir, B. Tahir, Z.Y. Zakaria, A. Muhammad, Enhanced photocatalytic carbon dioxide reforming of methane to fuels over nickel and montmorillonite supported TiO_2 nanocomposite under UV-light using monolith photoreactor, J. Clean. Prod. 213 (2019) 451–461.
[33] M. Madi, M. Tahir, Fabricating V_2AlC/g-C_3N_4 nanocomposite with MAX as electron moderator for promoting photocatalytic CO_2-CH_4 reforming to CO/H_2, Int. J. Energy Res. (2022) 1–20.
[34] S. Yin, L. Sun, Y. Zhou, X. Li, J. Li, X. Song, P. Huo, H. Wang, Y. Yan, Enhanced electron–hole separation in SnS_2/Au/g-C_3N_4 embedded structure for efficient CO_2 photoreduction, Chem. Eng. J. 406 (2021) 126776.
[35] H. Li, Y. Jing, X. Ma, T. Liu, L. Yang, B. Liu, S. Yin, Y. Wei, Y. Wang, Construction of a well-dispersed Ag/graphene-like g-C_3N_4 photocatalyst and enhanced visible light photocatalytic activity, RSC Adv. 7 (14) (2017) 8688–8693.
[36] I. Papailias, T. Giannakopoulou, N. Todorova, D. Demotikali, T. Vaimakis, C. Trapalis, Effect of processing temperature on structure and photocatalytic properties of g-C_3N_4, Appl. Surf. Sci. 358 (2015) 278–286.
[37] X. Wang, D. Zhang, H. Zhang, L. Gong, Y. Yang, W. Zhao, S. Yu, Y. Yin, D. Sun, In situ polymerized polyaniline/MXene (V_2C) as building blocks of supercapacitor and ammonia sensor self-powered by electromagnetic-triboelectric hybrid generator, Nano Energy 88 (2021) 106242.
[38] E. Ghasali, Y. Orooji, A. Azarniya, M. Alizadeh, M. Kazem-zad, Touradj Ebadzadeh, Production of V_2C MXene using a repetitive pattern of V_2AlC MAX phase through microwave heating of Al-V_2O_5-C system, Appl. Surf. Sci. 542 (2021) 148538.
[39] Q. Tang, Z. Sun, S. Deng, H. Wang, Z. Wu, Decorating g-C_3N_4 with alkalinized Ti_3C_2 MXene for promoted photocatalytic CO_2 reduction performance, J. Colloid Interface Sci. 564 (2020) 406–417.
[40] C. Yang, Q. Tan, Q. Li, J. Zhou, J. Fan, B. Li, J. Sun, K. Lv, 2D/2D Ti_3C_2 MXene/g-C_3N_4 nanosheets heterojunction for high efficient CO_2 reduction photocatalyst: dual effects of urea, Appl. Catal. B 268 (2020) 118738.
[41] M. Tahir, B. Tahir, 2D/2D/2D O-C_3N_4/Bt/Ti_3C_2Tx heterojunction with novel MXene/clay multi-electron mediator for stimulating photo-induced CO_2 reforming to CO and CH_4, Chem. Eng. J. 400 (2020) 125868.
[42] M. Tahir, B. Tahir, In-situ growth of TiO_2 imbedded $Ti_3C_2T_A$ nanosheets to construct PCN/$Ti_3C_2T_A$ MXenes 2D/3D heterojunction for efficient solar driven photocatalytic CO_2 reduction towards CO and CH_4 production, J. Colloid Interface Sci. 591 (2021) 20–37.
[43] Q. Wang, L. Zhang, Y. Guo, M. Shen, M. Wang, B. Li, J. Shi, Multifunctional 2D porous g-C_3N_4 nanosheets hybridized with 3D hierarchical TiO_2 microflowers for selective dye adsorption, antibiotic degradation and CO_2 reduction, Chem. Eng. J. 396 (2020) 125347.
[44] W.K. Fan, M. Tahir, Recent developments in photothermal reactors with understanding on the role of light/heat for CO_2 hydrogenation to fuels: a review, Chem. Eng. J. 427 (2022) 131617.

[45] X. Wang, Z. Wang, Y. Bai, L. Tan, Y. Xu, X. Hao, J. Wang, A.H. Mahadi, Y. Zhao, L. Zheng, Y.-F. Song, Tuning the selectivity of photoreduction of CO_2 to syngas over Pd/layered double hydroxide nanosheets under visible light up to 600 nm, J. Energy Chem. 46 (2020) 1–7.
[46] A. Bafaqeer, M. Tahir, N.A.S. Amin, A.R. Mohamed, M.A.C. Yunus, Fabricating 2D/2D/2D heterojunction of graphene oxide mediated g-C_3N_4 and ZnV_2O_6 composite with kinetic modelling for photocatalytic CO_2 reduction to fuels under UV and visible light, J. Mater. Sci. 56 (16) (2021) 9985–10007.
[47] S. Tasleem, M. Tahir, Investigating the performance of liquid and gas phase photoreactors for dynamic H_2 production over bimetallic TiO_2 and Ni_2P dispersed MAX Ti_3AlC_2 monolithic nanocomposite under UV and visible light, J. Environ. Chem. Eng. 9 (4) (2021) 105351.
[48] S. Tasleem, M. Tahir, Z.Y. Zakaria, Fabricating structured 2D Ti_3AlC_2 MAX dispersed TiO_2 heterostructure with Ni_2P as a cocatalyst for efficient photocatalytic H_2 production, J. Alloy. Compd. 842 (2020) 155752.
[49] M. Tahir, B. Tahir, Constructing S-scheme 2D/0D g-C_3N_4/TiO_2 NPs/MPs heterojunction with 2D-Ti_3AlC_2 MAX cocatalyst for photocatalytic CO_2 reduction to CO/CH_4 in fixed-bed and monolith photoreactors, J. Mater. Sci. Technol. 106 (2022) 195–210.
[50] M. Yang, P. Wang, Y. Li, S. Tang, X. Lin, H. Zhang, Z. Zhu, F. Chen, Graphene aerogel-based NiAl-LDH/g-C_3N_4 with ultratight sheet-sheet heterojunction for excellent visible-light photocatalytic activity of CO_2 reduction, Appl. Catal., B 306 (2022) 121065.
[51] S. Xiong, S. Bao, W. Wang, J. Hao, Y. Mao, P. Liu, Y. Huang, Z. Duan, Y. Lv, D. Ouyang, Surface oxygen vacancy and graphene quantum dots co-modified Bi_2WO_6 toward highly efficient photocatalytic reduction of CO_2, Appl. Catal. B 305 (2022) 121026.
[52] S. Xiao, Y. Guan, H. Shang, H. Li, Z. Tian, S. Liu, W. Chen, J. Yang, An S-scheme NH_2-UiO-66/SiC photocatalyst via microwave synthesis with improved CO_2 reduction activity, J. CO_2 Util. 55 (2022) 101806.
[53] M. Madi, M. Tahir, Highly stable $LaCoO_3$ perovskite supported g-C_3N_4 nanotextures with proficient charges migration for visible light CO_2 photoreduction to CO and CH_4, Mater. Sci. Semicond. Process. 142 (2022) 106517.
[54] A.A. Khan, M. Tahir, A.R. Mohamed, Constructing S-scheme heterojunction of carbon nitride nanorods (g-CNR) assisted trimetallic CoAlLa LDH nanosheets with electron and holes moderation for boosting photocatalytic CO_2 reduction under solar energy, Chem. Eng. J. 433 (2022) 133693.
[55] B. Tahir, M. Tahir, M.G.M. Nawawi, Highly stable 3D/2D WO_3/g-C_3N_4 Z-scheme heterojunction for stimulating photocatalytic CO_2 reduction by H_2O/H_2 to CO and CH_4 under visible light, J. CO_2 Util. 41 (2020) 101270.
[56] M. Tahir, Synergistic effect in MMT-dispersed Au/TiO_2 monolithic nanocatalyst for plasmon-absorption and metallic interband transitions dynamic CO_2 photoreduction to CO, Appl. Catal. B 219 (2017) 329–343.
[57] Q. He, H. Hu, Y. Shao, Z. Zhao, Switchable optical nonlinear properties of monolayer V_2CTX MXene, Optik 247 (2021) 167629.
[58] Y. Liu, Y. Jiang, Z. Hu, J. Peng, W. Lai, D. Wu, S. Zuo, J. Zhang, B. Chen, Z. Dai, Y. Yang, Y. Huang, W. Zhang, W. Zhao, W. Zhang, L. Wang, S. Chou, In-situ electrochemically activated surface vanadium valence in V_2C MXene to achieve high capacity and superior rate performance for Zn-ion batteries, Adv. Funct. Mater. 31 (8) (2020).
[59] Y. Feng, F. Zhou, M. Bo, Y. Huang, Q. Deng, C. Peng, Enabling high dielectric response in PVDF/V_2C MXene–TiO_2 composites based on nontypical V–F–Ti bonding and fermi-level overlapping mechanisms, J. Phys. Chem. C. 124 (50) (2020) 27780–27789.
[60] L. Wang, Z. Zhang, Q. Han, Y. Liu, J. Zhong, J. Chen, J. Huang, H. She, Q. Wang, Preparation of CdS-P25/ZIF-67 composite material and its photocatalytic CO_2 reduction performance, Appl. Surf. Sci. 584 (2022) 152645.
[61] C. Prasad, X. Yang, Q. Liu, H. Tang, A. Rammohan, S. Zulfiqar, G.V. Zyryanov, S. Shah, Recent advances in MXenes supported semiconductors based photocatalysts: Properties, synthesis and photocatalytic applications, J. Ind. Eng. Chem. 85 (2020) 1–33.